Structural basis of HSV-1 DNA replication origin-binding protein UL9

Cuiqing Huang[1,#], Haiqiang Wu[2,3,#], Jinmiao Song[2], Xinzheng Zhang[1,4,*], Jun Ma[2,*]

[1]State Key Laboratory of Biomacromolecules, Institute of Biophysics, Chinese Academy of Sciences, Beijing, 100101, China

[2]Institute of Infectious Diseases, Shenzhen Bay Laboratory, Shenzhen, 518132, China

[3]College of Veterinary Medicine, Anhui Agricultural University, Hefei, 230036, China

[4]University of Chinese Academy of Sciences, 100049 Beijing, China

[#]These authors contributed equally: Cuiqing Huang, Haiqiang Wu

*Correspondence: Jun Ma (majun@szbl.ac.cn), Xinzheng Zhang (xzzhang@ibp.ac.cn)

Abstract

The herpesvirus DNA replication machinery comprises a battery of viral enzymes that orchestrate viral genome synthesis. In HSV-1, the machinery consists of seven essential components, including the replication origin-binding protein UL9, ssDNA-binding protein ICP8, the heterodimeric DNA polymerase complex UL30/UL42, and the heterotrimeric helicase-primase complex UL5/UL8/UL52. UL9, an SF2 helicase family member, functions as a dimer that sequence-specifically recognizes the replication origin sites and unwinds duplex DNA to initiate replication. Furthermore, UL9 interacts with several viral replication components to recruit the replication machinery, as well as with cellular proteins that regulate its own functions. However, the molecule mechanisms underlying UL9's multifunctionality remain poorly understood due to the lack of structural information. In this study, we present the first cryo-EM structures of UL9 in both apo and DNA-bound states. Combining biochemical and enzymatic assays, we elucidate the molecular basis of UL9 dimerization, origin recognition and activity regulation by ICP8-binding.

Keywords

Herpesvirus, DNA replication machinery, Origin-Binding Protein, UL9, Helicase superfamily

Introduction

The *Herpesviridae* family is a large group of enveloped viruses with relatively large, complex double-stranded DNA genomes. To date, over 100 herpesviruses with a wide range of vertebrate hosts have been recognized and classified into three subfamilies (α-, β- and γ-herpesvirus) based on their biological properties and tissue tropism. Notably, nine herpesviruses are pathogenic in humans and cause numerous human diseases, these include α-herpesviruses (herpes simplex virus types 1 and 2 (HSV-1, HSV-2), varicella-zoster virus (VZV)); β-herpesviruses (human cytomegalovirus (HCMV), human herpesvirus 6A/B (HHV-6A, HHV-6B), human herpesvirus 7 (HHV-7)); γ-herpesviruses (Epstein-Barr virus (EBV) and Kaposi's sarcoma-associated herpesvirus (KSHV/HHV-8))[1]. Over 90% people around the world has been infected with various herpesviruses. These herpesviruses establish lifelong latency in infected persons and periodically reactivate during the episodes of immunosuppression or physiological stress, with no existing therapeutic approaches to achieve complete viral eradication[2]. Up to date, there are limited medical interventions to specific herpesviruses, including two launched vaccines Shingrix and Zostavax for VZV[3], and antiviral drugs such as Acyclovir, Valacyclovir, Famciclovir and Pritelivir effective against HSV-1 and VZV[4]. For other herpesviruses, particularly oncogenic pathogens EBV and KSHV, effective antiviral drugs or vaccines remain unavailable. Furthermore, currently antiviral drugs also carry the risks of side effects and drug resistance[4-6]. Therefore, developing new medical treatments against herpesviruses is essential. Viral DNA replication represents a particularly promising therapeutic target[7, 8].

In herpesviruses, viral DNA replication occurs in the nucleus of host cell and is carried out by a sophisticated multienzyme DNA replication machinery[9-11]. For HSV-1, its DNA replication machinery comprises seven core components, including the replication origin-binding protein (OBP) UL9, single-stranded DNA (ssDNA)-binding protein ICP8, the heterodimeric DNA polymerase complex UL30/UL42, and the heterotrimeric helicase-primase complex UL5/UL8/UL52. The DNA polymerase complex possesses two functionally distinct subunits: the catalytic subunit UL30 is a B-family DNA polymerase harboring both 5'-3' polymerase activity and 3'-5' proofreading exonuclease activity, and the processivity factor UL42 helps polymerase maintain the high processing ability. Within the

helicase-primase complex, the helicase subunit UL5 is responsible for double-stranded DNA (dsDNA) unwinding during elongation, the primase subunit UL52 synthesizes short RNA primers for DNA polymerase, and the primase-helicase associated factor UL8 coordinates the activities of UL5 and UL52. The ssDNA-binding protein ICP8 is a multifunctional protein that prefers to bind ssDNA in a non-sequence-specific and cooperative manner while preventing it from nuclease degradation and annealing. Additionally, ICP8 stimulates the helicase activity of UL9, modulates DNA polymerase processivity, and regulates helicase-primase complex function through direct interactions with UL9, UL42 and UL8[9-11], respectively. The origin-binding protein UL9 mainly orchestrates replication initiation through sequence-specific recognition of origin sites and subsequently unwinds the genomic DNA with the help of ICP8 to initiate DNA replication[9-18]. Furthermore, UL9 functions as a molecular hub, interacting with viral replication components ICP8[17, 19-21], UL42[22-24] and UL8[25] to recruit the replication machinery while engaging cellular proteins[11] such as topoisomerase I[21], hTid-1[26], and heat shock proteins[27] to regulate its own functions. These multifaceted roles establish UL9 as a central coordinator of herpesvirus DNA synthesis.

As a member of the SF2 helicase superfamily, HSV-1 UL9 has been reported to function as a dimer under physiological conditions[15, 28], possessing an N-terminal helicase domain and a C-terminal domain (Fig. 1a). Despite its essential role in HSV-1 DNA replication initiation, the understanding of UL9's molecular mechanism remains elusive due to the lack of structural information. In this study, we present the structures of HSV-1 UL9 in both apo and DNA-bound states, determined by cryo-electron microscopy (cryo-EM) single-particle analysis. Combined with *in vitro* biochemical and enzymatic assays, we elucidate the molecular basis of UL9's dimerization, origin recognition and activity regulation by ICP8 interaction. These findings not only advance our understanding of the mechanism of HSV-1 replication initiation but also provide potential new targets for the development of anti-herpesviral drugs.

91 # Result

92 ## Cryo-EM structure determination of HSV-1 UL9

93 For structural studies, the recombinant full-length HSV-1 UL9 ($UL9^{FL}$) protein was
94 expressed in insect cells using the Bac-to-Bac expression system and purified to
95 homogeneity through a tandem two-step purification (Supplementary Fig. 1). The UL9-DNA
96 complex was prepared by incubating affinity-purified UL9 with 56-bp dsDNA containing Box
97 I and II from OriS at a molar ratio of 1:1.5, followed by gel filtration (Supplementary Fig. 1).
98 Using cryo-EM single-particle analysis, the structures of apo-UL9 and the UL9-DNA
99 complex were resolved at resolutions of 4.1 Å and 3.7 Å (Fig. 1, Supplementary Figs. 2 and
100 3, and Supplementary Table 1), respectively. The model of UL9-DNA complex, which with
101 higher overall resolution, was first built with the help of the predicted models using
102 Alphafold 2[29] and mainly used for subsequent structural analyses. The final structural
103 model of the UL9-dsDNA complex comprises residues 19-843 and two duplex DNA
104 molecules, with residues 135-146, 267-283 and 431-456 missing (Fig. 1c and
105 Supplementary Fig. 4a). The region comprising residues 748-799 and duplex DNA was
106 flexible, resulting in a local resolution below 4.5 Å (Supplementary Figs. 2g). Accordingly,
107 the model for residues 748-799 and only 23-bp of the duplex DNA was constructed by
108 fitting the AlphaFold-predicted structure into the density map. Moreover, the nucleic acid
109 sequence in the model remained undetermined, which prevented subsequent analysis of
110 UL9's sequence-specific recognition mechanism. In contrast to the UL9-dsDNA complex,
111 residues 748-799 were not modeled in the apo-UL9 structure due to the complete absence
112 of corresponding density in the cryo-EM map (Supplementary Fig. 4b).

113

114 ## Architecture of the UL9 dimeric complex

115 Consistent with previous reports demonstrating UL9 is a dimer in solution and *in vivo*[15,
116 28], the resolved apo-UL9 and UL9-DNA complex are dimers with C2 symmetry. The
117 UL9-DNA complex displays overall dimensions of 115 × 110 × 65 Å (Supplementary Fig.
118 4a). In contrast, apo-UL9 structure obviously lacks bound DNA and DNA-binding elements,
119 leaving a slender yet compact structure core (Supplementary Fig. 4b). While the UL9 dimer
120 adopts a compact structure core, the protomers exhibit an extended architecture (Figs. 2a,
121 b). The extended conformation enables clear structural segmentation of UL9 into two

122 functional domains: the N-terminal helicase domain (residues 19-535) and C-terminal
123 domain (residues 536-851). The dimer interface is primarily formed by closely adjacent
124 CTDs, which constitute the rigid dimeric core, while the two helicase domains are located
125 on the either side of the core without any interaction between each other. Furthermore, no
126 significant conformational differences were observed between apo-UL9 and the UL9-DNA
127 complexes (Supplementary Fig. 4c).
128
129 **Structural details of UL9 helicase domain**
130 For N-terminal helicase domain of UL9, structural homology analysis was performed using
131 the Dali server[30]. The top hits of the identified structural homology including DDX48[31]
132 (PDB: 7ZNJ, Z=18.9, RMSD=3.8 Å) (Fig. 2c), DDX17[32] (PDB: 6UV3, Z=18.7, RMSD=3.9
133 Å) and Vasa[33] (PDB: 4D26, Z=15.9, RMSD=3.9 Å). And all these homologs belong to the
134 DExD/H-box SF2 helicase superfamily. Like the members of SF2 helicase superfamily,
135 UL9's helicase domain can be subdivided into two RecA-like subdomains, RecA1 (residues
136 40-242) and RecA2 (residues 243-406 and 476-501) (Figs. 1a and 2a-d). Structural
137 comparison of UL9's RecA1 and RecA2 subdomains with their counterparts in DDX48
138 (RecA1, residues 23-242; RecA2, residues 243-404) revealed root-mean-square deviation
139 (RMSD) values of 2.5 Å and 4.1 Å (Fig. 2d), respectively, indicating that UL9 maintains
140 conserved structural features of RecA-like domain with seven parallel β-strands. Key
141 residues implicated in ATP binding and hydrolysis within RecA1 are exactly the same, as
142 evidenced by the structural alignment of the AlphaFold-predicted UL9-ATP model with
143 DDX48 (Fig. 2e). By comparison, UL9's helicase domain possesses additional structural
144 elements (residues 19-39, 407-475 and 502-535) beyond the conserved RecA1 and RecA2
145 subdomains (Fig. 2d). The discontinuous fragments constitute a specific structure spanning
146 between RecA1 and RecA2, which we define as the **Bridge motif** (Fig. 2a-c). The Bridge
147 motif participates in UL9 dimerization and may also be involved in allosteric regulation of
148 UL9 function, as will be described later. This unique structural feature of UL9 exhibits
149 divergence from canonical SF2 family helicases, particularly the DExD/H-box subfamily.
150 Our observations imply that the herpesvirus UL9-like helicases have evolved unique
151 structural adaptations during viral evolution, potentially enabling novel molecular
152 mechanisms distinct from cellular SF2 helicases.

153

154 **Structural details of UL9 C-terminal domain**

155 The CTD can also be structurally subdivided into three subdomains or regions (Figs. 1 and
156 2a, b). **The first subdomain** (residues 536-747 and 800-833), comprising twelve α-helices
157 and two antiparallel β-sheet pairs, constitutes the structural core of CTD and mediates UL9
158 dimerization through extensive interactions with multiple regions of the opposing protomer.
159 Based on its functional characteristics, we designate this subdomain as the **C-terminal**
160 **dimerization domain (CDD)**. **The second subdomain** (residues 748-799) mainly
161 comprises four α-helices. Structural homology analysis using the Dali server[30] revealed
162 that only this subdomain of the CTD showed significant similarity to known domains. The
163 top structural homologs were all SAP (SAF-A/B, Acinus, PIAS) domains, including
164 MAFN[34] (PDB: 6HA7, Z=5.3, RMSD=2.7 Å), CDNF (PDB: 8QAJ, Z=4.6, RMSD=2.5 Å),
165 PIAS1[35] (PDB: 1V66, Z=3.9, RMSD=2.1 Å), and so on (Figs. 2f and Supplementary Fig.
166 5). Notably, these matches exhibited <15% sequence identity despite structural
167 conservation (Sequence identity between the residues 748-799 of UL9 and the SAP
168 domain of MANF is 12.8%.). The SAP domain, named after three founding members
169 SAF-A/B, Acinus and PIAS, represents a compact 35-residue module with a conserved
170 structural fold of two α-helices separated by a turn[36]. It is found in numerous nuclear and
171 cytoplasmic proteins participating in chromatin organization, transcriptional regulation, DNA
172 repair, and RNA metabolism, and well-characterized for its DNA/RNA-binding properties[36,
173 37] (Supplementary Fig. 5b). In UL9, this subdomain also functions as the determinant for
174 dsDNA binding, leading us to classify this DNA-binding motif as a **SAP domain**. **The third**
175 **structural region** comprises the last 17 residues (residues 834-851) located at the
176 extreme C-terminus, which protrudes from the core CDD domain. This flexible terminal
177 extension exhibits a tail-like structural conformation, therefore we named it the C-terminal
178 tail (**C-tail**). The C-tail facilitates UL9 dimerization, mediates ICP8 interactions, and
179 modulates UL9's activity, as detailed below.

180

181 **Structural details of UL9 dimerization**

182 Under physiological conditions, UL9 functions in the form of dimer[15, 28]. The dimerization
183 mechanism is not yet clear due to limited structural information[28]. In this study, the

184 purified UL9 proteins exist definitively as dimers in solution, in both apo and DNA-bound
185 states confirmed by the cryo-EM (Figs. 1b, c and Supplementary Fig. 2). Moreover, DNA
186 binding induces no observable conformational changes in the UL9 dimer structure
187 (Supplementary Fig. 4c). Structural analysis demonstrates that UL9 homodimerization is
188 primarily mediated by symmetric interactions between one protomer's CTD domain (only
189 the CDD subdomain and C-tail) and the opposing protomer's CDD subdomain and helicase
190 domain, with an overall interface area of approximately 3815 $Å^2$. Notably, no direct
191 interprotomer interactions were observed between the helicase domains. Furthermore, the
192 SAP domain shows no involvement in dimer formation.

193 According to the features of dimerization interface, we classified them into three types
194 (Fig. 3). **Type I interface** was located at the core of the dimer with C2 symmetry formed by
195 two adjacent CDD subdomains (Fig. 3b). It is formed mainly through hydrophobic
196 interactions, including the residues L552, A603, R606, H611, V616, L628, A630, P633,
197 L635, A823, I826, L827, A830, L831, and L834 from two protomers that form a hydrophobic
198 core. In addition, E555 and D824 of one protomer form additional a salt bridge and a
199 hydrogen bond with R607 of the other protomer, respectively, with E548 forming a
200 hydrogen bond with the main-chain of A603 (Supplementary Fig. 6a). **Type II interface** was
201 formed between the CDD subdomain of one protomer and the helicase domain of the
202 opposing protomer (Fig. 3c). The residues P596, M597, and P835 of the CDD subdomain
203 form van der Waals forces with the residues V410, F430, Y469, and C473 of the Bridge
204 motif. The residues T599, S602, E642, S832, and E833 the CDD subdomain formed salt
205 bridges or hydrogen bonds with N373 of RecA2, R406, S407, E408, P409, Q429 and Y469
206 of the Bridge motif, respectively (Supplementary Fig. 6b). **Type III interface** was created by
207 C-tail insertion into the inter-domain cleft formed by all subdomains of the helicase domain
208 and the CDD subdomain of the opposing protomer (Fig. 3d). The residue P835, A838,
209 W839, P840, M841, and M842 of C-tail form van der Waals forces with the residues V350,
210 V353, and P376 of RecA2, residues H468 and Y469 of Bridge, and residues A545, V550,
211 V554, V562, P564, and I567 of the CDD subdomain, residue T836, E837, A838, and Q843
212 form formed salt bridges or hydrogen bonds with residues R112, Y184, S185, and T187 of
213 RecA1, N373 of RecA2, R472 of Bridge, and N820 of CDD subdomain of the opposing
214 protomer (Supplementary Fig. 6c). Structurally, the C-tail serves as a molecular glue that

215 simultaneously tightly bridges multiple subdomains (RecA1, RecA2, Bridge and CDD) of
216 the opposing protomer and potentially inhibits the movement between subdomains. This
217 symmetric interaction between two protomers potentially stabilizes the UL9 dimer
218 conformation and contributes to allosteric regulation of its enzymatic activity.

219 Sequence alignment (Supplementary Figs. 7 and 8) indicated that interfaces I and II
220 are broadly conserved across most analyzed alphaherpesviruses or maintain conserved
221 biochemical properties. In contrast, interface III shows significantly higher conservation,
222 with 11 identical and 7 similar residues. Among human-infecting herpesviruses, while
223 interfaces I and II demonstrate high conservation within alpha or beta herpesviruses
224 respectively, clear divergence exists between the two subfamilies. Interface III retains
225 greater cross-subfamily conservation, preserving 7 identical and 5 similar residues. A
226 critical structural difference is the absence of the C-tail in beta herpesviruses, a functionally
227 important feature in alpha herpesviruses. These observations indicate that while the
228 dimerization mechanism remains relatively conserved between alpha and beta
229 herpesviruses, significant divergence has occurred in mechanistic details, particularly
230 regarding C-tail-mediated dimerization and functional regulation.

231

232 **Interaction details between UL9 and dsDNA**

233 The HSV-1 genome contains three distinct origin sites for viral DNA replication[9, 38].
234 UL9 specifically recognizes and binds to these origin sequences to initiate DNA
235 synthesis[13, 38, 39]. To elucidate the molecular mechanism of UL9-origin interaction, we
236 determined the cryo-EM structure of UL9-DNA complex. In UL9-DNA complex, UL9 binds
237 to dsDNA in a 2:2 stoichiometric ratio (Figs. 1b, c and Supplementary Figs. 9a, b).
238 Compared with apo-UL9, DNA binding induces no significant conformational changes,
239 except for the appearance of the SAP domain (Supplementary Figs. 2, 4). The structure of
240 UL9-DNA complex clearly reveals that dsDNA binding is almost restricted to the SAP
241 domain, with no other interactions observed elsewhere (Figs. 1b, c and Supplementary
242 Figs. 9a, b). Intriguingly, although the helicase domain possesses nucleic acid-binding
243 capability, no specific DNA binding to helicase domain was detected within the solved
244 structure.

245 Despite attempts to determine the sequence-specific recognition mechanism of UL9,

246 the flexibility of the SAP-DNA interaction region limited the local resolution of this part was
247 lower than 4.5 Å, preventing the acquisition of interaction details at the atomic level.
248 Structural analysis based on the AlphaFold-predicted model fitted into the low-resolution
249 density map reveals that UL9 likely interacts with dsDNA through residues Q749, R756,
250 K758, N759, K762, R783, Y786, M790, and K793 of SAP subdomain and residues K746,
251 K802 and R804 of CDD subdomain (Fig. 4a and Supplementary Fig. 9a). Residues R756,
252 K762, R783 and K793 of SAP and residues K746, K802 and R804 of CDD coordinate with
253 the phosphodiester backbone through ionic interactions. Residues Q749, N759, and K758
254 form hydrogen bonds with nucleobase edges. Residues Y786 and M790 stabilize base
255 stacking through van der Waals contacts (Fig. 4b). To pinpoint residues participating in DNA
256 interactions, we employed electrophoretic mobility shift assays (EMSA) for binding
257 confirmation and microscale thermophoresis (MST) assay for quantitative affinity
258 measurements. Since DNA binding is predominantly mediated by the SAP subdomain, all
259 assays were performed using the C-terminal domain of UL9 ($UL9^{CTD}$ or UL9C) and its
260 derived mutants. The dsDNA substrate used in EMSA and MST assays consisted of a
261 15-bp Box I sequence from OriS. The results of EMSA (Fig. 4c) demonstrated the deletion
262 of SAP ($UL9C^{\Delta SAP}$) and the triple mutant R756A/K758A/K762A ($UL9C^{mRKK}$) completely
263 abolished $UL9^{CTD}$-DNA interaction. Among single-point mutants, K746A, R756A, K758A,
264 K762A, Y786A, and M790A exhibited significant binding attenuation, whereas Q749A,
265 N759A, R783A, K793A, K802A and R804A mutants showed moderate but significant
266 reductions. MST assays (Supplementary Fig. 10) revealed that wild-type $UL9^{CTD}$ binds to
267 dsDNA with a dissociation constant (K_d) of 2.23 ± 0.42 μM. No binding was detected for
268 either $UL9C^{\Delta SAP}$ and $UL9C^{mRKK}$, while the binding affinities of mutants R756A, Y786A, and
269 M790A decreased by approximately 5- to 14-fold. Mutants K746A, K758A, K762A, K802A,
270 and R804A exhibited 2- to 4-fold reductions, and mutants Q749A, N759A, R783A, K793A
271 exhibited 1.4- to 1.8-fold reductions. Mutant R793A's binding ability is almost unaffected
272 due to its distal location within the DNA-binding interface. The results of MST assay are
273 consistent with those of EMSA, jointly identifying the residues involved in UL9-DNA
274 interactions. Collectively, dsDNA binding occurs through a coordinated mechanism
275 involving the SAP domain and three residues (K746, K802 and R804) within CDD
276 contiguous with SAP. These elements form a triangular SAP-CDD-dsDNA interaction

277 geometry (Fig. 4b) that stabilizes the SAP-DNA conformation, thereby facilitating SAP
278 domain visualization in the cryo-EM structure of the UL9-DNA complex.

279 Sequence alignment analysis reveals remarkable evolutionary conservation of
280 DNA-binding residues across α-herpesviruses (Supplementary Fig. 7). Especially, five
281 residues K758, N759, K762, Y786, and M790 exhibit absolute conservation across all
282 species examined, while four residues K746, R756, R783, and K793 consistently maintain
283 positively charged residues (Arg or Lys). Furthermore, three residues Q749, K802, and
284 R804 show restricted variability, with functionally distinct substitutions observed in one or
285 two of the ten analyzed species. Evolutionary conservation analysis of human
286 herpesvirus-encoded UL9-like proteins reveals distinct residue conservation profiles
287 (Supplementary Figure 8). Among human herpesvirus-encoded UL9-like proteins, distinct
288 conservation patterns are revealed (Supplementary Fig. 8). Residues K762 and K802
289 exhibit complete identity, while residues K758, R783, and K793 invariantly retain positively
290 charged side chains. N759 shows high conservation in five out of six species; the remaining
291 residues display significant divergence between α- and β-herpesvirus lineages.

292

293 **Structural basis underlying UL9-ICP8 interaction**

294 UL9 could interact with the ssDNA-binding protein ICP8 to form a ternary replication
295 initiation complex at the origin site[17, 40-42]. ICP8 has also been reported to stimulate the
296 helicase activity of UL9[17, 19, 20, 41]. While previous studies have identified the
297 C-terminus of UL9 as participating in ICP8 binding[17], the precise interaction site and
298 mechanism remain unclear. To map the minimal ICP8-interaction region of UL9, we
299 performed *in vitro* pull-down assays using recombinantly purified UL9 truncation mutants
300 based on the structural information. First, Strep-tag pull-down assay was employed to
301 compare the binding capacity of $UL9^{FL}$ and $UL9^{CTD}$ with ICP8. The results showed that
302 $UL9^{FL}$ displayed markedly weak interaction with ICP8, whereas $UL9^{CTD}$ exhibited strong
303 binding capacity (Fig. 5a). On this basis, we further investigated the specific region of
304 $UL9^{CTD}$ participated in interaction with ICP8. The GST pull-down assays showed that the
305 deletion of either the terminal 8 residue ($UL9C^{\Delta 8}$) or 16 residue ($UL9C^{\Delta 16}$) completely
306 abrogated the $UL9^{CTD}$-ICP8 interaction, while the isolated 8-residues (C-tail^{8aa}) or
307 16-residues (C-tail^{16aa}) segments showed no detectable ICP8-binding (Fig. 5b). The

308 deletion of SAP domain dose not impair the UL9C-ICP8 interaction, indicating that the SAP
309 domain is dispensable for ICP8 binding. These results demonstrate that both the CDD
310 subdomain and C-tail are cooperatively required for effective ICP8-binding.

311 Integrating the above findings with structural features of UL9, we propose a
312 mechanistic model for UL9-ICP8 interaction and its regulation. In the apo state of UL9, the
313 interaction between UL9 and ICP8 is severely impaired because the C-tail is wrapped by
314 the helicase domain of the opposing subunit, preventing cooperative engagement with the
315 CDD subdomain for ICP8 interaction. Conversely, in the functional state, UL9 must undergo
316 an ATP binding/hydrolysis-driven conformational rearrangement to release the C-tail,
317 thereby permitting its cooperative engagement with the CDD subdomain for greatly
318 enhenced ICP8 binding.

319

320 **Allosteric activation of UL9 activity by ICP8-binding**

321 The HSV-1 UL9 primarily functions to unwind viral genome DNA at the replication origin
322 through ATP hydrolysis-driven conformational changes, facilitated by ICP8-binding. By
323 integrating structural information to explore potential regulatory mechanisms of UL9 activity,
324 we systematically characterized UL9's ATPase and helicase activities under various
325 conditions using specific mutants.

326 The purified recombinant wild-type UL9 exhibits both ATPase and helicase activities
327 (Fig. 5c and Supplementary Fig. 11a). As expected, the ATP-binding-deficient mutant K87A
328 and hydrolysis-deficient mutant E175Q completely lost both ATPase and helicase activities,
329 confirming the essential role of ATP hydrolysis in UL9's molecular mechanism (Fig. 5c and
330 Supplementary Fig. 11a). The DNA-binding-deficient mutants $UL9^{\Delta SAP}$ and $UL9^{mRKK}$, which
331 maintain basal ATPase activity, show complete helicase deficiency due to abolished
332 DNA-binding capacity (Fig. 5c and Supplementary Fig. 11a). Furthermore, wild-type UL9
333 displays DNA-stimulated enhancement of ATPase activity, whereas mutants $UL9^{\Delta SAP}$ and
334 $UL9^{mRKK}$ fail to respond to DNA stimulation (Supplementary Fig. 11b). These findings
335 demonstrate that DNA-binding is not only essential for UL9's helicase activity but also
336 enhances its ATP hydrolysis.

337 We next investigated the functional impact of the UL9-ICP8 interaction on UL9's
338 ATPase and helicase activities. ATPase activity assays showed that UL9's ATP hydrolysis

339 rate increased progressively with rising ICP8 concentrations (Supplementary Fig. 11c).
340 Compared to wild-type UL9, both C-terminal truncation mutants UL9$^{\Delta 8}$ and UL9$^{\Delta 16}$ exhibited
341 enhanced ATPase activity in a progressive manner, with UL9$^{\Delta 8}$ exhibiting a 2.5-fold
342 increase and UL9$^{\Delta 16}$ a 1.5-fold increase (Fig. 5c). These findings align with previous
343 reports[39]. Meanwhile, increasing ICP8 concentration did not induce any significant
344 changes in the ATPase activity of either mutant (Supplementary Fig. 11c). These findings
345 indicate that C-terminal truncation increases ATPase activity while abolishing
346 ICP8-mediated regulation. Regarding helicase activity, the C-terminal truncation similarly
347 affected this function. In contrast to the observed enhancement in ATPase activity,
348 progressive truncation of the C-terminus led to a corresponding reduction in helicase
349 activity, with UL9$^{\Delta 8}$ displaying more pronounced impairment than UL9$^{\Delta 16}$ (Supplementary
350 Fig. 11a). While ICP8 remarkedly stimulated the helicase activity of wild-type UL9, both
351 truncation mutants showed no response to ICP8 stimulation (Fig. 5d).

352 Collectively, these results strengthen the implication of C-tail in UL9 dimerization, ICP8
353 interactions and the regulation of both ATPase and helicase activities. These findings are
354 consistent with the proposed role of C-tail as a molecular glue that tightly bridges multiple
355 subdomains of UL9, thereby limiting the mutual movement between subdomains which
356 potentially essential for UL9's activities. Since the interaction between C-tail and the
357 helicase domain overlaps with the potential nucleic acid-binding site, the dynamic
358 interaction between the C-tail and the helicase domain of the opposing protomer governs
359 the modulation of both ATPase and helicase activities.

360

361 ## Discussion

362 In summary, the cryo-EM structures of UL9 elucidate distinctive structural features and their
363 functional insights. While the N-terminal helicase domain's RecA subdomains maintain the
364 conserved features of SF2 helicases, UL9 uniquely possesses an evolutionary-derived
365 Bridge motif that distinguishes it from other SF2 helicase superfamily members. The
366 C-terminal domain exhibits a clear structural division into three functionally specialized
367 subdomains: (1) the CDD domain, principally mediating UL9 dimerization; (2) the SAP
368 domain, responsible for sequence specific recognition of the replication origin sites; and (3)

369 the C-tail, which participates in both UL9 dimerization and ICP8 interactions with potentially
370 playing crucial roles in the allosteric regulation of UL9's enzymatic activity.

371 HSV-1 UL9 is a member of the herpesvirus-specific OBP family. As both an
372 origin-binding protein and helicase, UL9 exhibits functional parallels to simian virus 40
373 (SV40) large tumor antigen (LTag)[43] and human papillomavirus (HPV) E1 protein[43].
374 However, unlike the SF3 helicase superfamily member LTag and E1 that form hexamers[43,
375 44] through their helicase domains, UL9 functions solely as a dimer mainly through its
376 unique CDD domain rather than helicase domain. Structural homology analysis shows that
377 the helicase domain of UL9 is most similar to the DExD/H-box SF2 helicase superfamily. In
378 addition, the key residues involved in ATP binding and hydrolysis are almost completely
379 conserved. However, UL9 displays several unique structural features. Unlike members of
380 the SF2 helicase superfamily, which generally function as monomers[45, 46], UL9 functions
381 as a dimer. In addition, the key residues of the core motif II of HSV-1 UL9 have undergone
382 evolutionary divergence: DEAH in Prp2 and DECH in HCV NS3 (both from the
383 DEAH/D-box subfamily), DEAD in DDX48 and eIF4A (DEAD-box subfamily), DEVH in Ski2
384 (Ski2-like subfamily), and DQAD in Vasa (Vasa subfamily). However, this contrasts with
385 174-DEVM-177 in HSV-1 UL9 as well as in HSV-2 and VZV, and its variant DEIM in
386 β-herpesviral UL9-like proteins (HHV6A, HHV6B and HHV7) (Supplementary Fig. 8).
387 Furthermore, an additional Bridge motif is present within the helicase domain. These
388 distinctive features clearly differentiate UL9 from well-characterized SF2 helicase
389 superfamily members. Given these unique structural and mechanistic properties, along with
390 the conservation of dimerization and DNA recognition among herpesvirus-encoded
391 UL9-like OBPs, we propose classifying all herpesviruses encoding UL9-like OBPs as a
392 distinct **UL9-like SF2 helicase subfamily**.

393 As a member of the SF2 helicase superfamily, UL9 contains a conserved helicase
394 domain exhibiting potential nucleic acid-binding capability (Supplementary Fig. 9). While
395 the solved UL9-DNA complex structure reveals that primary dsDNA binding occurs through
396 the SAP domain, this configuration alone fails to explain the duplex DNA unwinding
397 mechanism. We therefore propose that the helicase domain of UL9 may harbor an
398 additional DNA-binding site potentially exhibits specificity for ssDNA, as proposed in
399 previous literature[47, 48]. This putative DNA-binding site likely cooperates with SAP

domain to facilitate duplex DNA unwinding through ATP hydrolysis-induced conformational changes.

Combining the findings that ICP8 predominantly binds cooperatively to both the C-tail and the CDD subdomain of UL9 to stimulate both its ATPase and helicase activities, we propose the following **working model for UL9** (Fig. 6). Stage I, UL9 exists as a dimer in its resting state, with each protomer's C-tail inserted into the inter-domain cleft of the opposing protomer. This structural arrangement maintains the helicase domains in a low activity state with minimal ATP hydrolysis ability. Stage II, upon ICP8 binding to the C-tails of UL9, the C-tails are extracted from the inter-domain cleft, relieving auto-inhibition and activating the ATP hydrolysis ability of the helicase domains. Stage III, the activated helicase domains bind ssDNA and unwinds duplex DNA through ATP hydrolysis-driven conformational changes. Stage IV, following DNA unwinding, the ssDNA products are released and ICP8 dissociates from the UL9 complex.

While this study has elucidated the structural basis of UL9's dimerization, dsDNA recognition and ICP8-mediated activity regulation, the precise molecular mechanisms underlying its sequence-specific origin recognition and dsDNA unwinding remain unresolved. Future structural studies focused on UL9, particularly its complexes with origin DNA in different conformational states, the UL9-ICP8-DNA ternary complex, and its complexes with other viral or cellular partner proteins, are essential to fully elucidate the multifunctional mechanisms of UL9. Furthermore, the development of anti-herpesviral drugs targeting the structure and function of UL9 presents a promising avenue.

422 ## Materials and methods

423 ### DNA substrates and preparation

424 All DNA substrates used in this study were synthesized by Tsingke Biotechnology and
425 purified by HPLC. The oligonucleotides were initially dissolved in Annealing buffer (10 mM
426 Tris-HCl, pH 8.0, 50 mM NaCl, 1 mM EDTA) to a final concentration of 100 μM. For
427 preparation of unlabeled dsDNA or fork DNA, complementary strands were mixed at a 1:1
428 molar ratio. For FAM-labeled constructs, the labeled strand and its unlabeled
429 complementary strand were mixed at a 1:1.2 molar ratio. The mixtures were heated to 95°C
430 and denatured for 5 min in a thermal cycler (Bio-Rad), followed by gradual cooling to room
431 temperature at least 3 h with the thermal cycler lid open. The annealed DNA products were
432 stored at 4°C and used within one week.

433 dsDNA substrate containing Box I and II from OriS used in cryo-EM single particle analysis:

434 $F_{cryo\text{-}EM}$: 5'-AAGCGTTCGCACTTCGTCCCAATATATATATATTATTAGGGCGAAGTGCGAGCACT-3'

435 $R_{cryo\text{-}EM}$: 5'-AGTGCTCGCACTTCGCCCTAATAATATATATATATTGGGACGAAGTGCGAACGCTT-3'

436 dsDNA substrate containing Box I from OriS used in helicase and ATPase activity assay:

437 $F_{Helicase}$: 5'-CGCGAAGCGTTCGCACTTCGTCCTTTTTTTTTTTTTTTT-3'

438 $R_{Helicase}$: 5'-TTTTTTTTTTTTTTTTGGACGAAGTGCGAACGCTTCGCG-FAM-3'

439 15-bp dsDNA of Box I from OriS for MST assay and EMSA assay:

440 F_{MST}: 5'-GCGTTCGCACTTCGT-3'

441 R_{MST}: 5'-ACGAAGTGCGAACGC-3'

442

443 ### Protein expression and purification

444 The genes encoding full-length HSV-1 UL9 (UniProt: P10193) and ICP8 (UniProt: P04296)
445 were codon-optimized and synthesized (GeneralBiol). UL9 was cloned into the pFastBac-1
446 (Invitrogen) vector with an N-terminal Strep-tag (^{Strep}UL9) and expressed in Hi5 insect cells.
447 After 48 h post-infection with P3 baculovirus generated in Sf9 cells, cells were harvested by
448 centrifugation at 1500 × g for 10 min. The pellet was resuspended in Lysis Buffer (50 mM
449 HEPES, 500 mM NaCl, 10% glycerol, pH 7.0) supplemented with cOmplete (Roche). The
450 resuspended cells were sonicated for 15 min and centrifuged with a Beckman JA25.50
451 rotor at 20,000 × *g* for 40 min at 4 °C. The supernatant was retained and incubated
452 Strep-Tactin XT beads (IBA Lifesciences) for 1 h at 4 °C. The beads were then washed

453 three times with Lysis Buffer to remove non-specifically bound proteins, and target protein
454 was subsequently eluted using 2.5 mM D-biotin in Lysis Buffer. The target protein was
455 pooled supplemented with 1 mM DTT, concentrated (AmiconUltra, 50 kDa molecular mass
456 cut-off) (Millipore), and further purified using Superdex 200 Increase 10/300 GL column (GE
457 Healthcare) in Gel filtration buffer (20 mM HEPES, 300 mM NaCl, 1 mM DTT, pH 7.0).

458 The C-terminal domain of UL9 (residues 536-851, $UL9^{CTD}$) was cloned into pET-22b
459 vector (Novagen) with an N-terminal 8×His tag and overexpressed in *E. coli* BL21(DE3)
460 (Novagen) cells. Protein expression was induced at 16 °C for 16-20 h with 0.3 mM
461 isopropyl-1-thio-β-Dgalactopyranoside (IPTG) until OD600 ≈ 0.6. Cells harvested were
462 resuspended in Lysis Buffer and lysed by three passes through a microfluidizer. After
463 high-speed centrifugation at 20,000 × *g* for 40 min, the clarified supernatant was incubated
464 with Ni-NTA agarose (GE Healthcare) for 1 h at 4 °C. Beads were washed three times with
465 Lysis Buffer containing 60 mM imidazole, and target protein was eluted in Lysis Buffer
466 containing 300 mM imidazole. The eluted protein was pooled, concentrated (10 kDa
467 molecular mass cut-off), and further purified using Superdex 75 Increase 10/300 GL column
468 (GE Healthcare) in Gel filtration buffer. All $UL9^{CTD}$ mutants were purified using the same
469 protocol as wild-type. $UL9^{CTD}$ and its truncation mutants used for GST pull-down assays,
470 along with two C-tail fragments, were cloned into the pGEX-6P-1 vector (GE Healthcare) to
471 generate GST-tagged fusion proteins. Recombinant protein expression, cell resuspension,
472 and lysis procedures followed the same protocol as for His-tagged $UL9^{CTD}$. After
473 centrifugation, the clarified supernatants were incubated with Glutathione-Sepharose 4B
474 beads (GE Healthcare) at 4 °C for 1 h. The resin was then washed with Lysis buffer, and the
475 GST-tagged target proteins were eluted using GST elution buffer (50 mM HEPES, 300 mM
476 NaCl, 50 mM reduced glutathione, 1 mM DTT, pH 7.0). Finally, the eluted proteins were
477 analyzed using SDS-PAGE, concentrated, and buffer-exchanged into Gel filtration buffer for
478 subsequent analysis.

479 The full-length ICP8 was cloned into pFastBac-1 vector with an N-terminal 8×His tag
480 and overexpressed in insect cells using the same protocol as $UL9^{FL}$. Cell harvesting,
481 resuspension, and lysis also followed the procedure outlined for $UL9^{FL}$. ICP8 was purified
482 via Ni-NTA affinity chromatography as $UL9^{CTD}$, and then used for biochemical studies.

483 To prepare the UL9-dsDNA complex, purified UL9 and pre-treated dsDNA were mixed

484 at a 1:1.5 molar ratio in 150 mM NaCl and incubated for 1 h on ice. The mixture was further
485 purified using Superdex 200 Increase 10/300 GL column in buffer containing 20 mM
486 HEPES, 150 mM NaCl, 1 mM DTT, pH 7.0 (Supplementary Fig. 1). Fractions containing the
487 target complex were pooled and concentrated, and the fresh sample was used immediately
488 for structural studies.
489

490 **Cryo-EM grid preparation and date collection**

491 For cryo-EM grid preparation, freshly concentrated UL9 and UL9-dsDNA complex were first
492 diluted to 0.6 mg ml^{-1} and 0.8 mg ml^{-1}, respectively. The cryo-EM grids were prepared using
493 an automatic plunge freezer Vitrobot Mark IV (ThermoFisher Scientific) under 100%
494 humidity at 4 °C. Each aliquot of 3 μl diluted UL9 or UL9-dsDNA complex was loaded onto
495 the freshly glow-discharged NiTi grid (R1.2/1.3, 300 mesh, Zhenjiang Lehua). After
496 incubation for 10 s, excess sample was blotted with filter paper for 3 s with a blot force of 3,
497 and then the grid was vitrified by flash plunging into liquid ethane. All datasets were
498 automatically collected using SerialEM[49] through the beam-image shift data collection
499 method[50] on a 300 kV Titan Krios microscope (ThermoFisher Scientific) equipped with an
500 energy filter and a K2 Summit detector (Gatan). Images were recorded under the
501 super-resolution mode at a nominal magnification of 165,000× and a defocus value ranged
502 between -1.0 to -3.0 μm, resulting in a pixel size of 0.41 Å. Each move stack was exposed
503 for 6.2 s with a total exposure dose of ~60 electrons per $Å^2$ over 32 frames.
504

505 **Data processing and reconstruction**

506 All cryo-EM movie stacks were firstly binned and subjected to beam-induced motion
507 correction and anisotropic magnification correction using MotionCor2[51]. Contrast transfer
508 function (CTF) parameters were estimated with CTFFIND4.1[52] using non-dose-weighted
509 images. Subsequent processing steps, including particle picking, 2D classification, 3D
510 classification, and auto-refinement were performed in Relion-3.08[53] using dose-weighted
511 images. First, particles were automatic picked using the Laplacian-of-Gaussian filter and
512 processed with several rounds of reference-free 2D classification. Then, the best five
513 images with clear structural features and diverse orientations were selected as templates
514 for reference-based particle auto-picking. For apo-UL9, a total of 1,090,101 particles were

515 picked from 2080 micrographs and subjected to reference-free 2D classification. 249,188
516 particles with clear structural features were kept for further 3D classification with C2
517 symmetry imposed, using the initial model generated by Relion. One among the five
518 classes containing 158,949 particles were selected for final 3D auto-refinement, resulting in
519 a 4.1 Å resolution density map (Supplementary Fig. 2). For UL9-DNA complex, 913,885
520 particles were picked from 2055 micrographs. After 2D classification, 147,241 particles
521 were selected for further 3D classification with C2 symmetry, using the density map of
522 apo-UL9 as the initial model. 110,702 particles from the best class among five was
523 subjected to 3D auto-refinement and resulted in a 3.7 Å resolution density map
524 (Supplementary Fig. 2). The local resolutions of final maps were calculated using
525 ResMap[54]. Statistics for data collection and processing were summarized in
526 Supplementary Table S1.
527

528 **Model building and refinement**

529 For model building, the UL9-dsDNA complex was first built in Coot[55] with the help of the
530 predicted model from Alphafold 2[29] based on it higher resolution and better quality
531 density map. The cryo-EM density map of C-termianl domain (residues 536-844) in the
532 UL9-dsDNA complex was good enough to trace almost all the residues; however, some
533 density was missing at the N-terminal helicase domain (residues 19-535). The complete
534 model was further improved by a few iterative rounds of real-space refinement using
535 PHENIX[56] and manual modification in Coot until no further improvement could be
536 achieved. The apo-UL9 model was generated by docking the refined mode of UL9-dsDNA
537 complex into the corresponding density map in UCSF ChimeraX[57], followed by iterative
538 real-space refinement and manual modification. The final model of UL9-dsDNA complex
539 includes residues 19-843 and two duplex DNA molecules, with residues 135-146, 267-283
540 and 431-456 missing. In contrast, residues 748-799 in the apo-UL9 model was not modeled
541 due to the absence of corresponding density in the cryo-EM map. Statistics of the final
542 models were summarized in Supplementary Table S1. Structural analysis was performed
543 with UCSF ChimeraX and PyMOL (https://pymol.org/).
544

545 **ATPase activity assay**

546 ATPase activity assays were performed using the Malachite Green Phosphate Detection Kit
547 (Beyotime) according to the manufacturer's instructions. The reactions were carried out by
548 mixing 1 μM UL9 protein and 2.5 mM ATP of the final concentration in 20 μl ATPase Buffer
549 (20 mM HEPES, pH 7.5, 150 mM NaCl, 5mM $MgCl_2$, 1 mM DTT, 10% glycerol) in 96-well
550 plates and incubated at 37 ^{o}C for 30 min. The reactions were terminated by adding 180 μl
551 200 mM EDTA , followed by addition of 70 μl malachite green reagent for colorimetric
552 detection, and further incubated at room temperature for 30 min. The absorbance values of
553 colorimetric products were measured at 630 nm using an Envison Multimode Microplate
554 Reader (PerkinElmer). The phosphate standard curve was prepared according to the kit
555 instructions. All assays were independently repeated at least three times.
556
557 **Helicase activity assay**
558 FAM-labeled DNA substrates used for helicase activity assays were prepared by annealing
559 a 3'-FAM-labeled DNA with an unlabeled complementary DNA at a mole ratio of 1:1.2. The
560 reactions were carried out by mixing 50 nM dsDNA or fork DNA substrate with proteins of
561 different concentrations in Helicase Buffer (20 mM HEPES, pH 7.5, 150 mM NaCl, 1 mM
562 DTT, 10% glycerol, 5 mM $MgCl_2$, 0.1% BSA, 2.5 mM ATP) and incubated at 37 °C for 30
563 min. The reactions were terminated by adding 1 mg/ml proteinase K for 20 min. The
564 samples were analyzed using 15% Uera-PAGE and the images were taken using a
565 ChemiDoc^{TM} MP Imaging System (Bio-Rad). All assays were independently repeated at
566 least three times.
567
568 **Electrophoretic Mobility Shift Assay (EMSA)**
569 DNA binding of UL9^{CTD} was analyzed using Electrophoretic Mobility Shift assay (EMSA).
570 Briefly, 0.5-3.5 μM of purified UL9^{CTD} or its mutants were incubated with 40 nM FAM-labeled
571 dsDNA for 1 h at 4 °C in 20 μl EMSA buffer (50 mM Tris, pH 8.0, 50 mM NaCl, 1 mM DTT).
572 Then the samples were mixed with loading dye and analyzed by 7% non-denaturing PAGE
573 gel in 1 × TG buffer (25 mM Tris, 192 mM glycine). The gels were imaged using a
574 ChemiDoc^{TM} MP Imaging System (Bio-Rad) according to the manufacturer instructions. All
575 assays were independently repeated at least three times.
576

577 **Microscale thermophoresis (MST) assay**

578 The dsDNA binding affinity of $UL9^{CTD}$ was performed using microscale thermophoresis
579 (MST) assay on a Monolith NT.115 instrument (NanoTemper Technologies). Purified $UL9^{CTD}$
580 or its mutants (Ligands) with serial dilution in MST buffer (50 mM Tris, pH 8.0, 150 mM NaCl,
581 1 mM DTT and 0.05% Tween-20) was mixed with 40 nM of FAM-labeled dsDNA (Target) as
582 using in EMSA assay. The samples were loaded into premium coated capillaries
583 (NanoTemper) after 30 min incubation in dark at room temperature. Measurements were
584 performed at 25 °C with 20% LED power and Medium MST power with laser off/on times of
585 5 s and 10 s, respectively. Data were collected using MO.Control software (v3.0), and
586 analyses using MO.Affinity Analysis 3 (v3.0) (NanoTemper) performed by fitting the
587 normalized fluorescence (F_{norm}) versus protein concentration to a single-site binding model.
588 All assays were independently repeated three times.

589

590 **Pull-down assay**

591 For GST pull-down assays, 50 μg of purified GST-fused $UL9^{CTD}$ mutants or C-tail peptides
592 were mixed with an equal amount of ICP8. After a tenth of each mixture was taken out as
593 input controls, 25 μl of prepared GST beads (GE Healthcare) and 1 ml Pull-down buffer (50
594 mM Tris, pH 8.0, 150 mM NaCl, 1 mM DTT and 0.05% Tween-20) were added to the
595 remaining samples and incubated with gentle rotation for 1 h at 4 °C. The beads were then
596 pelleted by centrifugation at 1,000 × *g* and washed three times with 1 ml Pull-down buffer,
597 and subsequently analyzed using 12% SDS-PAGE gels stained with Coomassie blue. For
598 Strep-tag pull-down assays, 50 μg of purified Strep-tagged $UL9^{CTD}$ or full-length UL9 were
599 mixed with an equal amount of ICP8. Subsequent steps were performed as described for
600 the GST pull-down assay. All assays were independently repeated three times.

601

602 ## Data availability

603 The cryo-EM density maps and corresponding atomic coordinates have been deposited in
604 the Electron Microscopy Data Bank (EMDB) and Protein Data Bank (PDB), respectively:
605 UL9 (PDB 9VJI, EMD-65114) and UL9-DNA complex (PDB 9VJH, EMD-65113). All data
606 that support the findings of this study are available from the corresponding authors on
607 reasonable request. Source data are provided with this paper.

References:

1. Lu L, Fan M, Li X, Su W, Wang X, Xue Y, et al. Herpesvirus-associated diseases: biomarkers and advancements in clinical research. Virol J. 2025;22(1):177. Epub 20250602. doi: 10.1186/s12985-025-02795-7. PubMed PMID: 40457345; PubMed Central PMCID: PMCPMC12128367.
2. Grinde B. Herpesviruses: latency and reactivation - viral strategies and host response. J Oral Microbiol. 2013;5. Epub 20131025. doi: 10.3402/jom.v5i0.22766. PubMed PMID: 24167660; PubMed Central PMCID: PMCPMC3809354.
3. Molero Garcia JM, Moreno Guillen S, Rodriguez-Artalejo FJ, Ruiz-Galiana J, Canton R, De Lucas Ramos P, et al. Status of Herpes Zoster and Herpes Zoster Vaccines in 2023: A position paper. Rev Esp Quimioter. 2023;36(3):223-35. Epub 20230208. doi: 10.37201/req/004.2023. PubMed PMID: 36752132; PubMed Central PMCID: PMCPMC10238794.
4. Piret J, Boivin G. Antiviral resistance in herpes simplex virus and varicella-zoster virus infections: diagnosis and management. Curr Opin Infect Dis. 2016;29(6):654-62. doi: 10.1097/QCO.0000000000000288. PubMed PMID: 27306564.
5. Whitley R, Baines J. Clinical management of herpes simplex virus infections: past, present, and future. F1000Res. 2018;7. Epub 20181031. doi: 10.12688/f1000research.16157.1. PubMed PMID: 30443341; PubMed Central PMCID: PMCPMC6213787.
6. Zinser E, Krawczyk A, Muhl-Zurbes P, Aufderhorst U, Drassner C, Stich L, et al. A new promising candidate to overcome drug resistant herpes simplex virus infections. Antiviral Res. 2018;149:202-10. Epub 20171115. doi: 10.1016/j.antiviral.2017.11.012. PubMed PMID: 29155164.
7. Bazhulina NP, Surovaya AN, Gursky YG, Andronova VL, Moiseeva ED, Nikitin CA, et al. Complex of the herpes simplex virus type 1 origin binding protein UL9 with DNA as a platform for the design of a new type of antiviral drugs. J Biomol Struct Dyn. 2014;32(9):1456-73. Epub 20130724. doi: 10.1080/07391102.2013.820110. PubMed PMID: 23879454; PubMed Central PMCID: PMCPMC4066892.
8. Font M, Sanmartin C, Alonso ML, Gracia L, Losa MJ, Marquiegui B, et al. New antiherpetic 1,3-phenylene derivatives, inhibitors of the interaction of the HSV-1 origin binding protein (OBP) with DNA. Drug Des Discov. 2000;16(4):295-315. PubMed PMID: 10807035.
9. Muylaert I, Tang KW, Elias P. Replication and recombination of herpes simplex virus DNA. J Biol Chem. 2011;286(18):15619-24. Epub 20110301. doi: 10.1074/jbc.R111.233981. PubMed PMID: 21362621; PubMed Central PMCID: PMCPMC3091170.
10. Weller SK, Coen DM. Herpes simplex viruses: mechanisms of DNA replication. Cold Spring Harb Perspect Biol. 2012;4(9):a013011. Epub 20120901. doi: 10.1101/cshperspect.a013011. PubMed PMID: 22952399; PubMed Central PMCID: PMCPMC3428768.
11. Packard JE, Dembowski JA. HSV-1 DNA Replication-Coordinated Regulation by Viral and Cellular Factors. Viruses. 2021;13(10). Epub 20211007. doi: 10.3390/v13102015. PubMed PMID: 34696446; PubMed Central PMCID: PMCPMC8539067.
12. Elias P, O'Donnell ME, Mocarski ES, Lehman IR. A DNA binding protein specific for an origin of replication of herpes simplex virus type 1. Proc Natl Acad Sci U S A. 1986;83(17):6322-6. doi: 10.1073/pnas.83.17.6322. PubMed PMID: 3018724; PubMed Central PMCID: PMCPMC386495.
13. Olivo PD, Nelson NJ, Challberg MD. Herpes simplex virus DNA replication: the UL9 gene encodes an origin-binding protein. Proc Natl Acad Sci U S A. 1988;85(15):5414-8. doi: 10.1073/pnas.85.15.5414. PubMed PMID: 2840659; PubMed Central PMCID: PMCPMC281767.
14. Weir HM, Calder JM, Stow ND. Binding of the herpes simplex virus type 1 UL9 gene product to an origin of viral DNA replication. Nucleic Acids Res. 1989;17(4):1409-25. doi: 10.1093/nar/17.4.1409. PubMed PMID: 2537958; PubMed Central PMCID: PMCPMC331812.

15. Fierer DS, Challberg MD. Purification and characterization of UL9, the herpes simplex virus type 1 origin-binding protein. J Virol. 1992;66(7):3986-95. doi: 10.1128/JVI.66.7.3986-3995.1992. PubMed PMID: 1318393; PubMed Central PMCID: PMCPMC241201.
16. Boehmer PE, Dodson MS, Lehman IR. The herpes simplex virus type-1 origin binding protein. DNA helicase activity. J Biol Chem. 1993;268(2):1220-5. PubMed PMID: 8380408.
17. Boehmer PE, Lehman IR. Physical interaction between the herpes simplex virus 1 origin-binding protein and single-stranded DNA-binding protein ICP8. Proc Natl Acad Sci U S A. 1993;90(18):8444-8. doi: 10.1073/pnas.90.18.8444. PubMed PMID: 8397405; PubMed Central PMCID: PMCPMC47373.
18. Stabell EC, Olivo PD. A truncated herpes simplex virus origin binding protein which contains the carboxyl terminal origin binding domain binds to the origin of replication but does not alter its conformation. Nucleic Acids Res. 1993;21(22):5203-11. doi: 10.1093/nar/21.22.5203. PubMed PMID: 8255778; PubMed Central PMCID: PMCPMC310638.
19. Boehmer PE. The herpes simplex virus type-1 single-strand DNA-binding protein, ICP8, increases the processivity of the UL9 protein DNA helicase. J Biol Chem. 1998;273(5):2676-83. doi: 10.1074/jbc.273.5.2676. PubMed PMID: 9446572.
20. Arana ME, Haq B, Tanguy Le Gac N, Boehmer PE. Modulation of the herpes simplex virus type-1 UL9 DNA helicase by its cognate single-strand DNA-binding protein, ICP8. J Biol Chem. 2001;276(9):6840-5. Epub 20001208. doi: 10.1074/jbc.M007219200. PubMed PMID: 11112774.
21. Makhov AM, Lee SS, Lehman IR, Griffith JD. Origin-specific unwinding of herpes simplex virus 1 DNA by the viral UL9 and ICP8 proteins: visualization of a specific preunwinding complex. Proc Natl Acad Sci U S A. 2003;100(3):898-903. Epub 20030124. doi: 10.1073/pnas.0237171100. PubMed PMID: 12552114; PubMed Central PMCID: PMCPMC298698.
22. Monahan SJ, Grinstead LA, Olivieri W, Parris DS. Interaction between the herpes simplex virus type 1 origin-binding and DNA polymerase accessory proteins. Virology. 1998;241(1):122-30. doi: 10.1006/viro.1997.8953. PubMed PMID: 9454723.
23. Trego KS, Parris DS. Functional interaction between the herpes simplex virus type 1 polymerase processivity factor and origin-binding proteins: enhancement of UL9 helicase activity. J Virol. 2003;77(23):12646-59. doi: 10.1128/jvi.77.23.12646-12659.2003. PubMed PMID: 14610187; PubMed Central PMCID: PMCPMC262563.
24. Trego KS, Zhu Y, Parris DS. The herpes simplex virus type 1 DNA polymerase processivity factor, UL42, does not alter the catalytic activity of the UL9 origin-binding protein but facilitates its loading onto DNA. Nucleic Acids Res. 2005;33(2):536-45. Epub 20050126. doi: 10.1093/nar/gki196. PubMed PMID: 15673714; PubMed Central PMCID: PMCPMC548344.
25. McLean GW, Abbotts AP, Parry ME, Marsden HS, Stow ND. The herpes simplex virus type 1 origin-binding protein interacts specifically with the viral UL8 protein. J Gen Virol. 1994;75 (Pt 10):2699-706. doi: 10.1099/0022-1317-75-10-2699. PubMed PMID: 7931156.
26. Eom CY, Lehman IR. The human DnaJ protein, hTid-1, enhances binding of a multimer of the herpes simplex virus type 1 UL9 protein to oris, an origin of viral DNA replication. Proc Natl Acad Sci U S A. 2002;99(4):1894-8. doi: 10.1073/pnas.042689499. PubMed PMID: 11854491; PubMed Central PMCID: PMCPMC122290.
27. Tanguy Le Gac N, Boehmer PE. Activation of the herpes simplex virus type-1 origin-binding protein (UL9) by heat shock proteins. J Biol Chem. 2002;277(7):5660-6. Epub 20011115. doi: 10.1074/jbc.M108316200. PubMed PMID: 11711536.
28. Chattopadhyay S, Weller SK. Direct interaction between the N- and C-terminal portions of the herpes simplex virus type 1 origin binding protein UL9 implies the formation of a head-to-tail dimer. J Virol.

698 2007;81(24):13659-67. Epub 20071017. doi: 10.1128/JVI.01204-07. PubMed PMID: 17942532; PubMed
699 Central PMCID: PMCPMC2168873.
700 29. Jumper J, Evans R, Pritzel A, Green T, Figurnov M, Ronneberger O, et al. Highly accurate protein
701 structure prediction with AlphaFold. Nature. 2021;596(7873):583-9. Epub 20210715. doi:
702 10.1038/s41586-021-03819-2. PubMed PMID: 34265844; PubMed Central PMCID: PMCPMC8371605.
703 30. Holm L. Dali server: structural unification of protein families. Nucleic Acids Res. 2022;50(W1):W210-W5.
704 doi: 10.1093/nar/gkac387. PubMed PMID: 35610055; PubMed Central PMCID: PMCPMC9252788.
705 31. Pacheco-Fiallos B, Vorlander MK, Riabov-Bassat D, Fin L, O'Reilly FJ, Ayala FI, et al. mRNA recognition
706 and packaging by the human transcription-export complex. Nature. 2023;616(7958):828-35. Epub 20230405.
707 doi: 10.1038/s41586-023-05904-0. PubMed PMID: 37020021; PubMed Central PMCID: PMCPMC7614608.
708 32. Ngo TD, Partin AC, Nam Y. RNA Specificity and Autoregulation of DDX17, a Modulator of MicroRNA
709 Biogenesis. Cell Rep. 2019;29(12):4024-35 e5. doi: 10.1016/j.celrep.2019.11.059. PubMed PMID: 31851931;
710 PubMed Central PMCID: PMCPMC6953907.
711 33. Xiol J, Spinelli P, Laussmann MA, Homolka D, Yang Z, Cora E, et al. RNA clamping by Vasa assembles a
712 piRNA amplifier complex on transposon transcripts. Cell. 2014;157(7):1698-711. Epub 20140605. doi:
713 10.1016/j.cell.2014.05.018. PubMed PMID: 24910301.
714 34. Yan Y, Rato C, Rohland L, Preissler S, Ron D. MANF antagonizes nucleotide exchange by the
715 endoplasmic reticulum chaperone BiP. Nat Commun. 2019;10(1):541. Epub 20190201. doi:
716 10.1038/s41467-019-08450-4. PubMed PMID: 30710085; PubMed Central PMCID: PMCPMC6358605.
717 35. Okubo S, Hara F, Tsuchida Y, Shimotakahara S, Suzuki S, Hatanaka H, et al. NMR structure of the
718 N-terminal domain of SUMO ligase PIAS1 and its interaction with tumor suppressor p53 and A/T-rich DNA
719 oligomers. J Biol Chem. 2004;279(30):31455-61. Epub 20040508. doi: 10.1074/jbc.M403561200. PubMed
720 PMID: 15133049.
721 36. Aravind L, Koonin EV. SAP - a putative DNA-binding motif involved in chromosomal organization. Trends
722 Biochem Sci. 2000;25(3):112-4. doi: 10.1016/s0968-0004(99)01537-6. PubMed PMID: 10694879.
723 37. Walker JR, Corpina RA, Goldberg J. Structure of the Ku heterodimer bound to DNA and its implications
724 for double-strand break repair. Nature. 2001;412(6847):607-14. doi: 10.1038/35088000. PubMed PMID:
725 11493912.
726 38. Olsson M, Tang KW, Persson C, Wilhelmsson LM, Billeter M, Elias P. Stepwise evolution of the herpes
727 simplex virus origin binding protein and origin of replication. J Biol Chem. 2009;284(24):16246-55. Epub
728 20090407. doi: 10.1074/jbc.M807551200. PubMed PMID: 19351883; PubMed Central PMCID:
729 PMCPMC2713539.
730 39. Murata LB, Dodson MS. The herpes simplex virus type 1 origin-binding protein. sequence-specific
731 activation of adenosine triphosphatase activity by a double-stranded DNA containing box I. J Biol Chem.
732 1999;274(52):37079-86. doi: 10.1074/jbc.274.52.37079. PubMed PMID: 10601266.
733 40. Manolaridis I, Mumtsidu E, Konarev P, Makhov AM, Fullerton SW, Sinz A, et al. Structural and biophysical
734 characterization of the proteins interacting with the herpes simplex virus 1 origin of replication. J Biol Chem.
735 2009;284(24):16343-53. Epub 20090327. doi: 10.1074/jbc.M806134200. PubMed PMID: 19329432; PubMed
736 Central PMCID: PMCPMC2713556.
737 41. Lee SS, Lehman IR. The interaction of herpes simplex type 1 virus origin-binding protein (UL9 protein)
738 with Box I, the high affinity element of the viral origin of DNA replication. J Biol Chem. 1999;274(26):18613-7.
739 doi: 10.1074/jbc.274.26.18613. PubMed PMID: 10373472.
740 42. Boehmer PE, Craigie MC, Stow ND, Lehman IR. Association of origin binding protein and single strand
741 DNA-binding protein, ICP8, during herpes simplex virus type 1 DNA replication in vivo. J Biol Chem.
742 1994;269(46):29329-34. PubMed PMID: 7961904.

743 43. Shahid T, Danazumi AU, Tehseen M, Alhudhali L, Clark AR, Savva CG, et al. Structural dynamics of DNA
744 unwinding by a replicative helicase. Nature. 2025;641(8061):240-9. Epub 20250319. doi:
745 10.1038/s41586-025-08766-w. PubMed PMID: 40108462; PubMed Central PMCID: PMCPMC12043514.
746 44. Javed A, Major B, Stead JA, Sanders CM, Orlova EV. Unwinding of a DNA replication fork by a
747 hexameric viral helicase. Nat Commun. 2021;12(1):5535. Epub 20210920. doi: 10.1038/s41467-021-25843-6.
748 PubMed PMID: 34545080; PubMed Central PMCID: PMCPMC8452682.
749 45. Cordin O, Banroques J, Tanner NK, Linder P. The DEAD-box protein family of RNA helicases. Gene.
750 2006;367:17-37. Epub 20051207. doi: 10.1016/j.gene.2005.10.019. PubMed PMID: 16337753.
751 46. Fairman-Williams ME, Guenther UP, Jankowsky E. SF1 and SF2 helicases: family matters. Curr Opin
752 Struct Biol. 2010;20(3):313-24. Epub 20100422. doi: 10.1016/j.sbi.2010.03.011. PubMed PMID: 20456941;
753 PubMed Central PMCID: PMCPMC2916977.
754 47. Marintcheva B, Weller SK. Helicase motif Ia is involved in single-strand DNA-binding and helicase
755 activities of the herpes simplex virus type 1 origin-binding protein, UL9. J Virol. 2003;77(4):2477-88. doi:
756 10.1128/jvi.77.4.2477-2488.2003. PubMed PMID: 12551986; PubMed Central PMCID: PMCPMC141079.
757 48. Macao B, Olsson M, Elias P. Functional properties of the herpes simplex virus type I origin-binding
758 protein are controlled by precise interactions with the activated form of the origin of DNA replication. J Biol
759 Chem. 2004;279(28):29211-7. Epub 20040508. doi: 10.1074/jbc.M400371200. PubMed PMID: 15133043.
760 49. Mastronarde DN. Automated electron microscope tomography using robust prediction of specimen
761 movements. J Struct Biol. 2005;152(1):36-51. doi: 10.1016/j.jsb.2005.07.007. PubMed PMID: 16182563.
762 50. Wu C, Huang X, Cheng J, Zhu D, Zhang X. High-quality, high-throughput cryo-electron microscopy data
763 collection via beam tilt and astigmatism-free beam-image shift. J Struct Biol. 2019;208(3):107396. Epub
764 20190925. doi: 10.1016/j.jsb.2019.09.013. PubMed PMID: 31562921.
765 51. Zheng SQ, Palovcak E, Armache JP, Verba KA, Cheng Y, Agard DA. MotionCor2: anisotropic correction
766 of beam-induced motion for improved cryo-electron microscopy. Nat Methods. 2017;14(4):331-2. Epub
767 20170227. doi: 10.1038/nmeth.4193. PubMed PMID: 28250466; PubMed Central PMCID:
768 PMCPMC5494038.
769 52. Rohou A, Grigorieff N. CTFFIND4: Fast and accurate defocus estimation from electron micrographs. J
770 Struct Biol. 2015;192(2):216-21. Epub 20150813. doi: 10.1016/j.jsb.2015.08.008. PubMed PMID: 26278980;
771 PubMed Central PMCID: PMCPMC6760662.
772 53. Zivanov J, Nakane T, Forsberg BO, Kimanius D, Hagen WJ, Lindahl E, et al. New tools for automated
773 high-resolution cryo-EM structure determination in RELION-3. Elife. 2018;7. Epub 20181109. doi:
774 10.7554/eLife.42166. PubMed PMID: 30412051; PubMed Central PMCID: PMCPMC6250425.
775 54. Kucukelbir A, Sigworth FJ, Tagare HD. Quantifying the local resolution of cryo-EM density maps. Nat
776 Methods. 2014;11(1):63-5. Epub 20131110. doi: 10.1038/nmeth.2727. PubMed PMID: 24213166; PubMed
777 Central PMCID: PMCPMC3903095.
778 55. Emsley P, Lohkamp B, Scott WG, Cowtan K. Features and development of Coot. Acta Crystallogr D Biol
779 Crystallogr. 2010;66(Pt 4):486-501. Epub 20100324. doi: 10.1107/S0907444910007493. PubMed PMID:
780 20383002; PubMed Central PMCID: PMCPMC2852313.
781 56. Adams PD, Afonine PV, Bunkoczi G, Chen VB, Davis IW, Echols N, et al. PHENIX: a comprehensive
782 Python-based system for macromolecular structure solution. Acta Crystallogr D Biol Crystallogr. 2010;66(Pt
783 2):213-21. Epub 20100122. doi: 10.1107/S0907444909052925. PubMed PMID: 20124702; PubMed Central
784 PMCID: PMCPMC2815670.
785 57. Pettersen EF, Goddard TD, Huang CC, Meng EC, Couch GS, Croll TI, et al. UCSF ChimeraX: Structure
786 visualization for researchers, educators, and developers. Protein Sci. 2021;30(1):70-82. Epub 20201022. doi:
787 10.1002/pro.3943. PubMed PMID: 32881101; PubMed Central PMCID: PMCPMC7737788.

58. Sievers F, Wilm A, Dineen D, Gibson TJ, Karplus K, Li W, et al. Fast, scalable generation of high-quality protein multiple sequence alignments using Clustal Omega. Mol Syst Biol. 2011;7:539. Epub 20111011. doi: 10.1038/msb.2011.75. PubMed PMID: 21988835; PubMed Central PMCID: PMCPMC3261699.

59. Robert X, Gouet P. Deciphering key features in protein structures with the new ENDscript server. Nucleic Acids Res. 2014;42(Web Server issue):W320-4. Epub 20140421. doi: 10.1093/nar/gku316. PubMed PMID: 24753421; PubMed Central PMCID: PMCPMC4086106.

Acknowledgements

Cryo-EM data collection was carried out at the Center for Biological Imaging (CBI), Core Facilities for Protein Science at the Institute of Biophysics (IBP), Chinese Academy of Sciences (CAS). We thank Boling Zhu, Xujing Li and other staff members at the CBI for their support with data collection. We thank Mengsi Sun from the Biochemistry core of Shenzhen Bay Laboratory for technical support for MST analysis. The project was funded by the National Key R&D Program of China (2021YFA1301501, 2017YFA0504700), the National Natural Science Foundation of China (31930069), the Strategic Priority Research Program of the Chinese Academy of Sciences (XDB37040101), the Basic Research Program Based on Major Scientific Infrastructures, CAS (JZHKYPT-2021-05), and the Key Laboratory of Biomacromolecules, Chinese Academy of Sciences (ZGD- 2023- 05). J.M. is supported by the Shenzhen Bay Laboratory Startup Fund (21330061) and the Beijing Nova Program (No. Z201100006820033).

Author contributions

J.M. and X.Z. conceived the project and designed all the experiments. C.H., H.W. and J.S. performed protein expression and purification, conducted biochemical and functional studies. C.H. prepared and screened the cryo-EM specimens. J.M. and C.H. collected and processed the cryo-EM data, and built the model. C.H., J.M. and X.Z. wrote the manuscript with input from all authors. All authors participated in experimental discussions, performed data analysis and interpretation, and approved the final version of the manuscript.

Competing interests

The authors declare no competing interests.

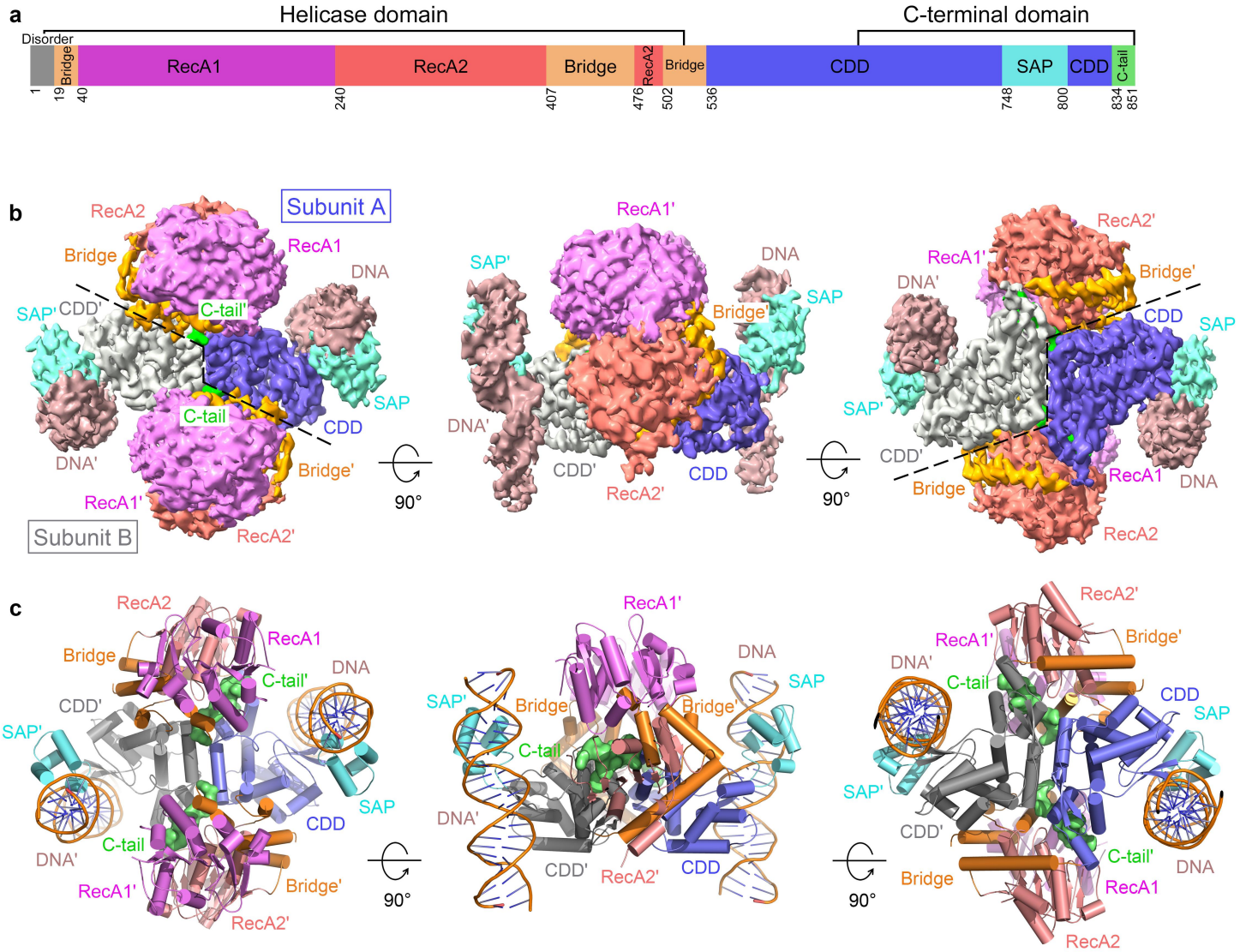

Figure 1. Cryo-EM structure of the UL9-DNA complex. a Domain architecture of HSV-1 UL9 protein, with the N-terminal helicase domain and C-terminal domain indicated. The RecA1, RecA2, Bridge, CDD, SAP and C-tail subdomains or regions are shown in violet, salmon, orange, slate, aquamarine and lime, respectively. Inter-subdomain boundaries are marked with residue numbers. **b** Three orthogonal views of the cryo-EM density map for the UL9-DNA complex, colored according to the domain coloring scheme in (**a**). **c** Corresponding orthogonal views of the atomic model presented in cartoon representation, colored identically to panel **b**.

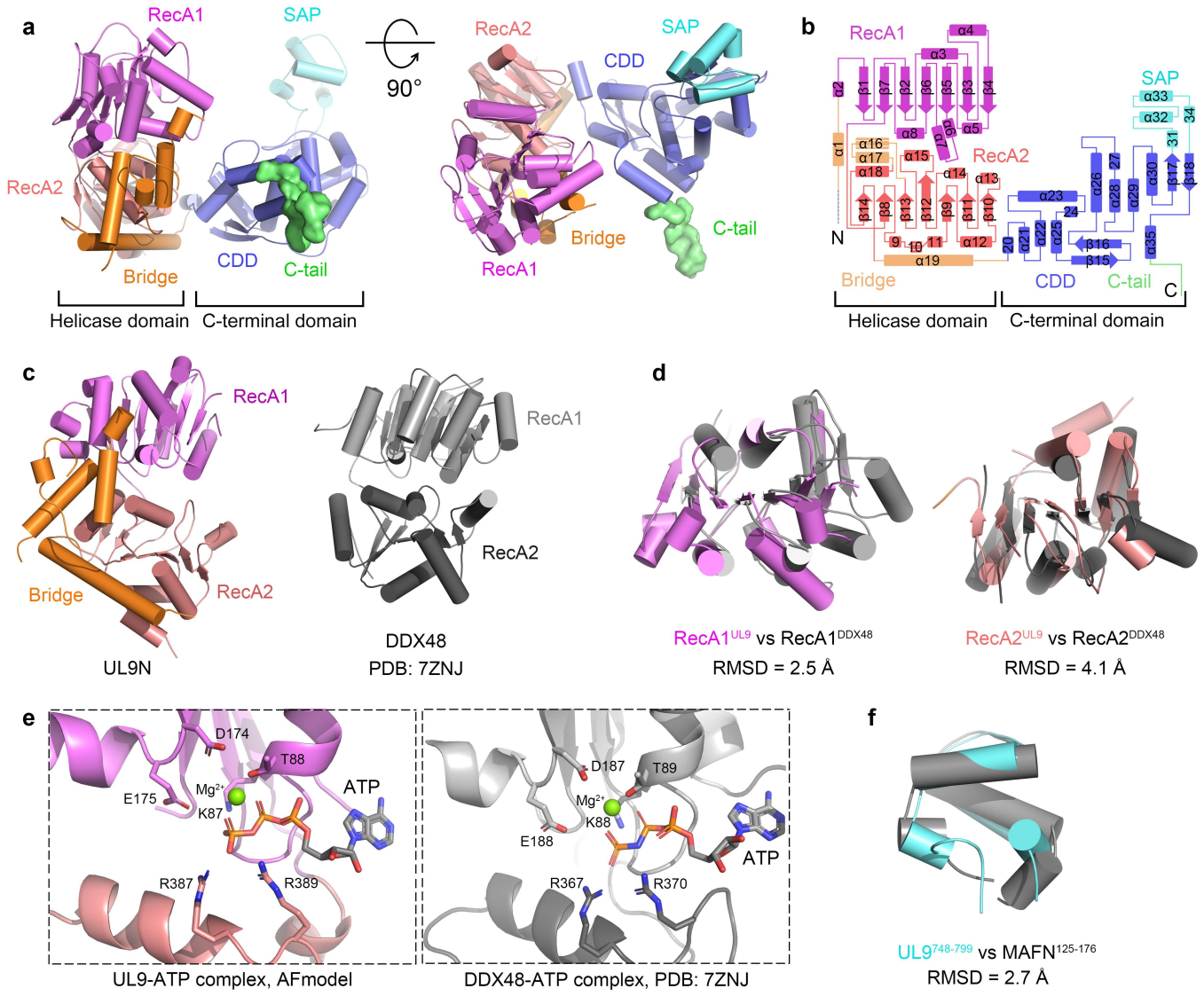

Figure 2. Structural analysis of UL9 protomer. a Two orthogonal views of the UL9 protomer structure. **b** Two-dimensional topology diagram of UL9. **c** Structural comparison of UL9 helicase domain with its structural homolog DDX48 identified by the Dali server. **d** Structural superposition of UL9 RecA1 and RecA2 subdomains with corresponding subdomains in DDX48. **e** Key residues involved in ATP binding and hydrolysis in UL9 are identical to those in its structural homolog DHX48. The UL9-ATP complex model was predicted with AlphaFold. **f** Structural superposition of UL9 SAP domain with its homolog MAFN identified by the Dali server. All structural representations throughout the panels follow the color scheme in Figure 1a, with domains labeled and homologous proteins (DDX48 and MAFN) shown in gray. RMSD values for structural superpositions in panels **d** and **f** are provided.

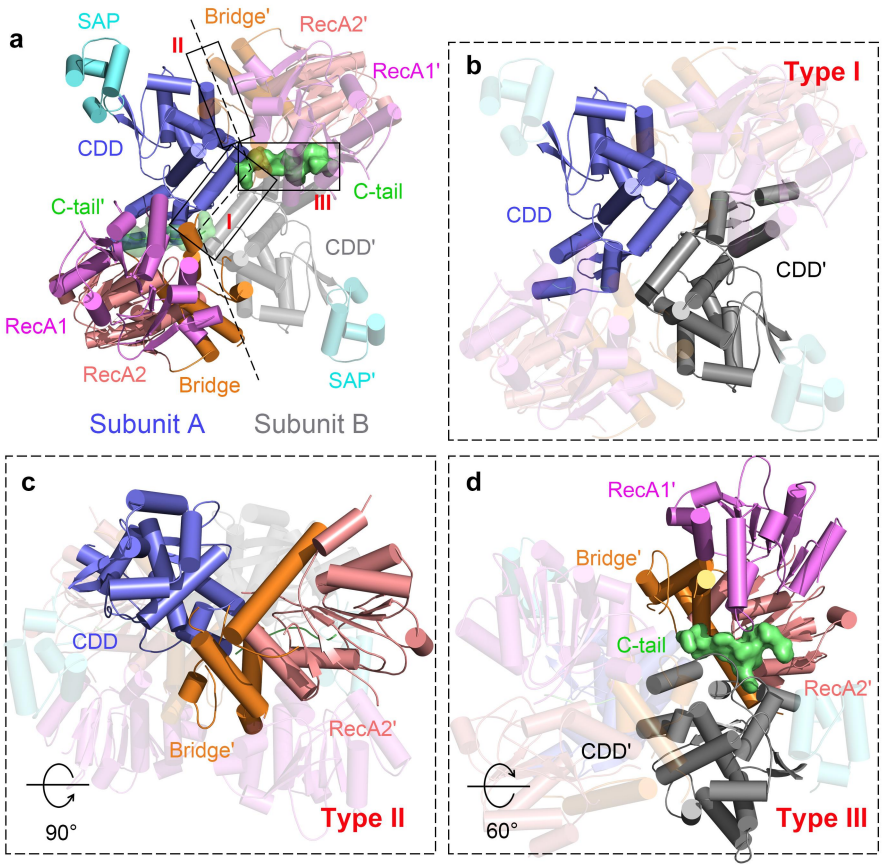

Figure 3. Structural details of UL9 dimerization. a Three types of dimerization interfaces classified in UL9. The two protomers are separated by a dashed line, with interfaces highlighted by solid rectangles and labeled. **b** Symmetrical Type I interface formed between CDDs. **c** Type II interface involving the CDD of one protomer and the RecA2 subdomain and Bridge motif of the opposing protomer. **d** Type III interface comprising the C-tail of one protomer and multiple subdomains (RecA1, RecA2, Bridge and CDD) of the opposing protomer. In panels **b-d**, subdomains involved in interactions are represented as cartoons with labels, whereas regions without interaction are shown as transparent cartoons.

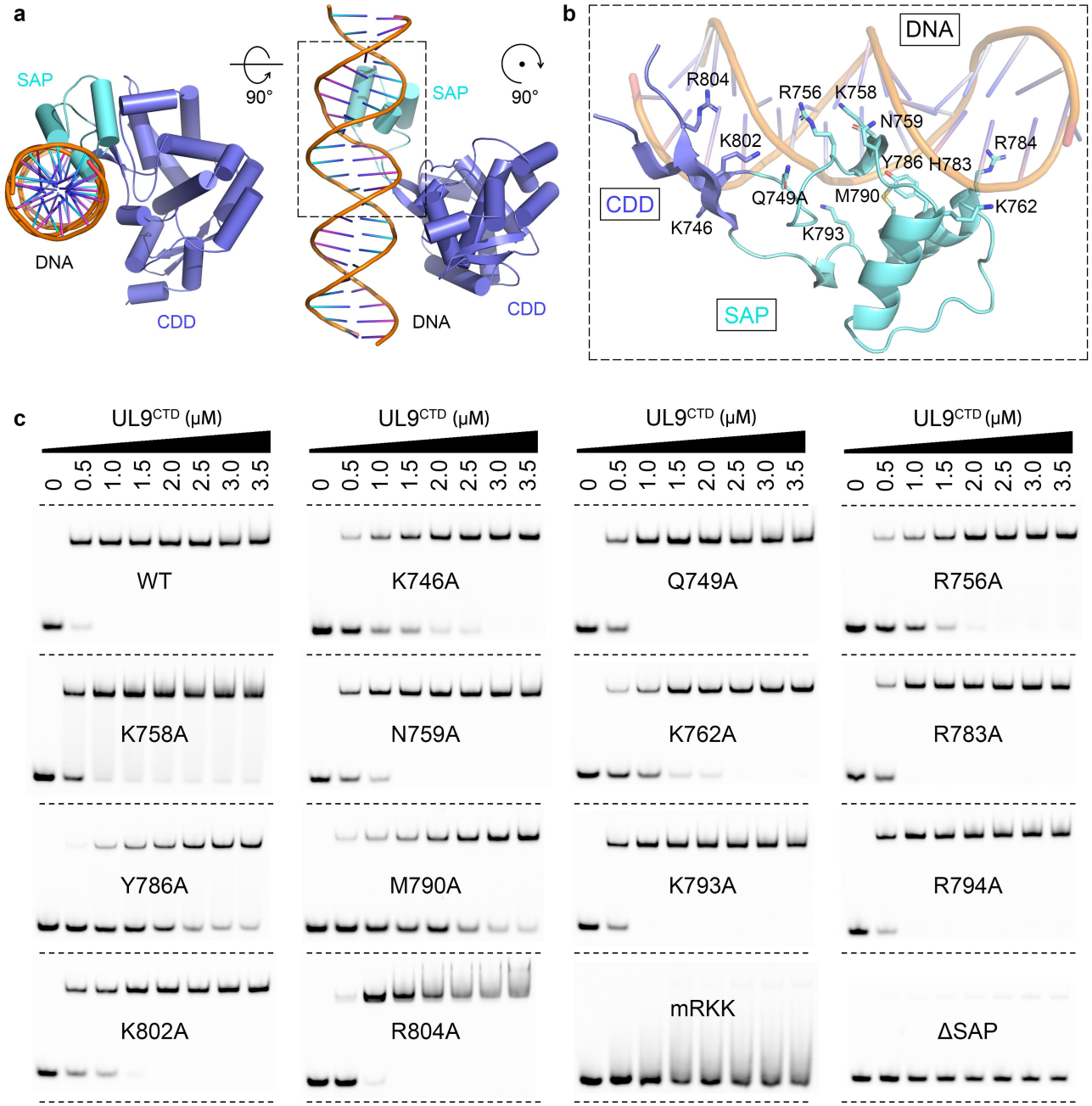

Figure 4. Details of the interaction between UL9 and DNA. a Two orthogonal views of the core structure of UL9-DNA interaction. **b** Structural details of UL9-DNA interaction. Panel **b** is an enlargement of the area enclosed by a dashed rectangle in panel **a** after rotation. Protein and DNA structures are represented as cartoons, with side chains of residues involved in UL9-DNA interactions displayed as sticks. **c** EMSA analysis of wild-type UL9^{CTD} and its potential DNA-binding mutants. For EMSA assay, a series of seven increasing UL9^{CTD} concentrations (ranging from 0.5 to 3.5 μM) were tested. All assays were independently repeated at least three times with consistent results.

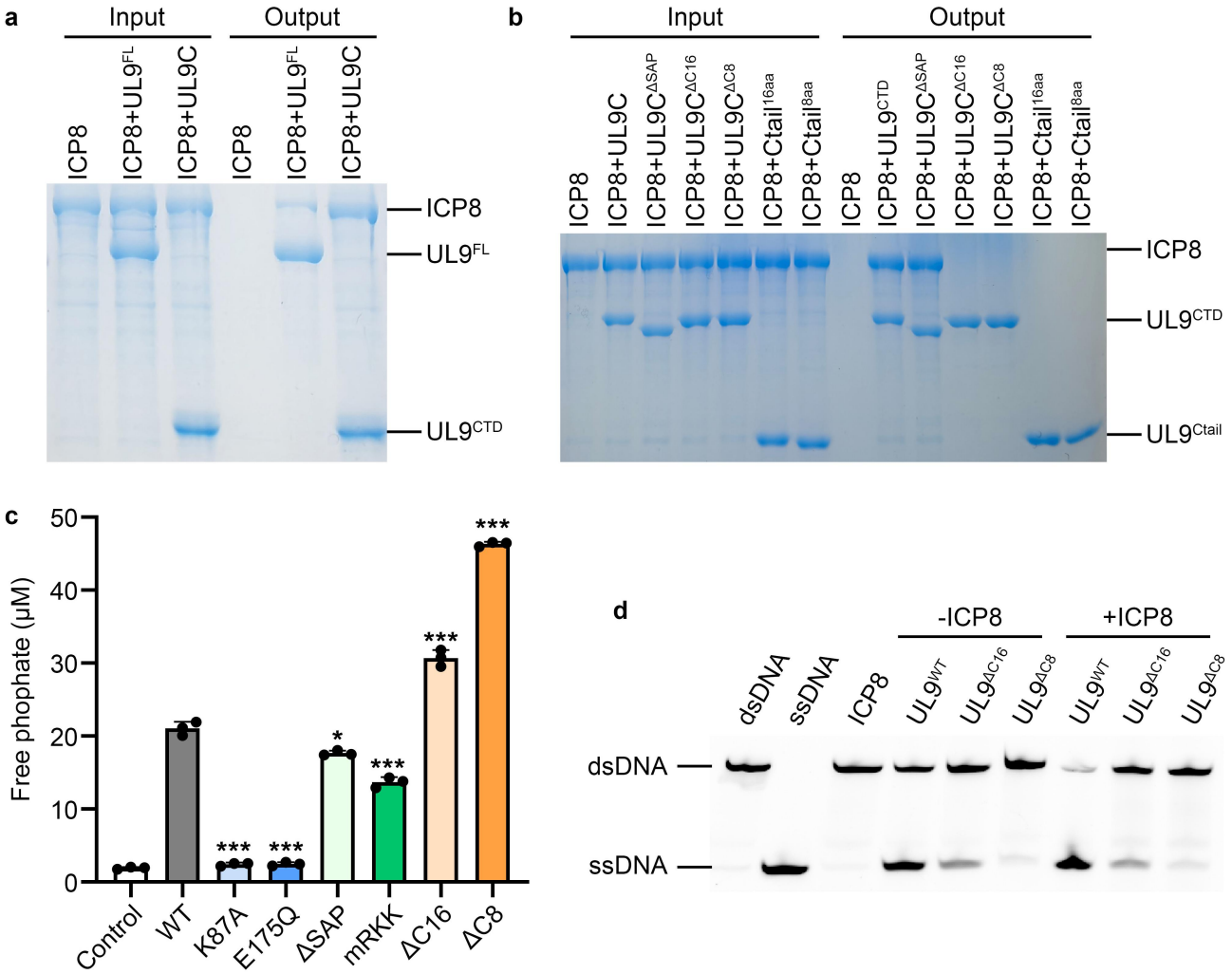

Figure 5. Interaction between UL9 and ICP8. a Strep-tag pull-down assay demonstrating interaction of ICP8 with either full-length UL9 or UL9^{CTD}. **b** GST pull-down assay analyzing binding between ICP8 and either UL9^{CTD} or the C-tail. **c** Comparative ATPase activity of wild-type UL9 versus its functional mutants. ATPase activity assays were performed using the Malachite Green Phosphate Detection Kit. Data are presented as the mean with standard deviation for experiments performed in triplicate. Statistical significance was determined by a two-tailed Student's *t*-test (*p < 0.05, **p < 0.01, *p < 0.001). **d** ICP8-mediated stimulation of UL9 helicase activity. Wild-type UL9 and two C-terminal truncation mutants (ΔC16 and ΔC8) were tested.

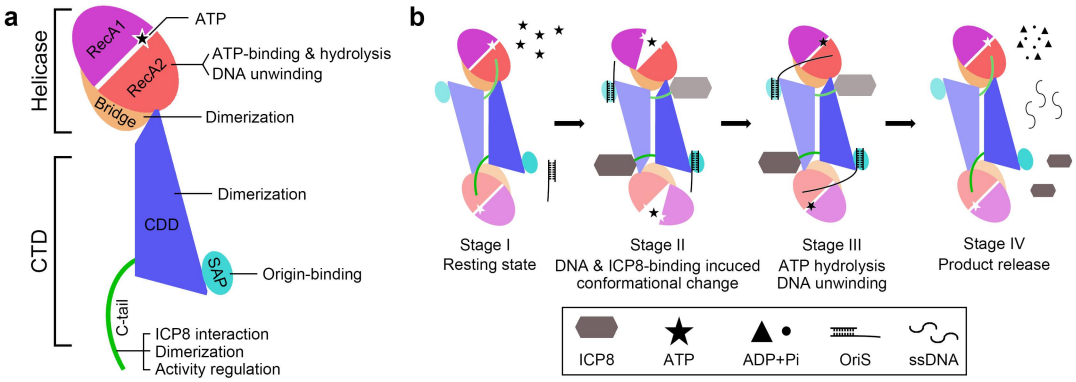

Figure 6. Working model of UL9 function. a A schematic diagram of HSV-1 UL9 showing domain organization and functional annotation. **b** Proposed catalytic cycle of UL9, divided into four stages. Stage 1, apo-UL9 dimer in resting conformation. Stage 2, conformational changes in UL9 dimeric complex induced by ICP8 and ATP binding, while dsDNA from the replication origin site binds to the SAP subdomain. Stage 3, coordinated ATP hydrolysis and ICP8 stimulation mediate dsDNA unwinding. Stage 4, release of reaction products (ADP and ssDNA), and ICP8 dissociation and recycling. Molecular component annotations are shown in the solid box below.